

Double-layer cross-shaped cylinder terahertz all-dielectric metasurface with a high quality factor and giant chiral response governed by bound states in the continuum

Xinrui Guo(郭昕蕊), Jingwei Lv(吕靖薇), Chao Liu(刘超), Qin Yu(俞钦), Jianing Shi(时佳宁), Qiang Liu(刘强), Jianxin Wang(王建鑫), Wei Liu(刘伟), and Paul K. Chu(朱剑豪)

Citation: Chin. Phys. B, 2026, 35 (**6**): 067801. DOI: 10.1088/1674-1056/ae516d
http://cpb.iphy.ac.cn; http://iopscience.iop.org/cpb

What follows is a list of articles you may be interested in

Topological edge state coupled mode-induced tetra-band tunable spin-dependent perfect absorption

Ji-Peng Wu(伍计鹏), Xi-Rui Zeng(曾玺瑞), Yu-Lei Liao(廖煜磊), Rong-Zhou Zeng(曾荣周), Hong Wen(文鸿), Xiao-Yu Dai(戴小玉), and Yuan-Jiang Xiang(项元江)

Chin. Phys. B, 2026, 35 (**4**): 047801. DOI: 10.1088/1674-1056/ae00b2

Design and implementation of the monochromator shielding for the cold neutron spectrometers XINGZHI and BOYA

Jinchen Wang(汪晋辰), Juanjuan Liu(刘娟娟), Daye Xu(徐大业), Florian Grünauer, Lijie Hao(郝丽杰), Yuntao Liu(刘蕴韬), Hongxia Zhang(张红霞), Peng Cheng(程鹏), and Wei Bao(鲍威)

Chin. Phys. B, 2024, 33 (**5**): 057801. DOI: 10.1088/1674-1056/ad3629

Designing radiative cooling metamaterials for passive thermal management by particle swarm optimization

Shenshen Yan(闫申申), Yan Liu(刘岩), Zi Wang(王子), Xiaohua Lan(兰晓华), Yi Wang(汪毅), and Jie Ren(任捷)

Chin. Phys. B, 2023, 32 (**5**): 057802. DOI: 10.1088/1674-1056/acc061

A flexible ultra-broadband metamaterial absorber working on whole K-bands with polarization-insensitive and wide-angle stability

Tao Wang(汪涛), He-He He(何贺贺), Meng-Di Ding(丁梦迪), Jian-Bo Mao(毛剑波), Ren Sun(孙韧), and Lei Sheng(盛磊)

Chin. Phys. B, 2022, 31 (**3**): 037804. DOI: 10.1088/1674-1056/ac306e

Faraday rotations, ellipticity, and circular dichroism in magneto-optical spectrum of moiré superlattices

J A Crosse and Pilkyung Moon

Chin. Phys. B, 2021, 30 (**7**): 077803. DOI: 10.1088/1674-1056/ac051f

---

Double-layer cross-shaped cylinder terahertz all-dielectric metasurface with a high quality factor and giant chiral response governed by bound states in the continuum

Xinrui Guo(郭昕蕊)[1], Jingwei Lv(吕靖薇)[1,†], Chao Liu(刘超)[1], Qin Yu(俞钦)[2], Jianing Shi(时佳宁)[1], Qiang Liu(刘强)[1], Jianxin Wang(王建鑫)[1], Wei Liu(刘伟)[1], and Paul K. Chu(朱剑豪)[3]

[1] *School of Physics and Electronic Engineering, Northeast Petroleum University, Daqing* 163318, *China*
[2] *Dewert OKIN Technology Group Co., Ltd., Jiaxing* 314015, *China*
[3] *Department of Physics, Department of Materials Science and Engineering, and Department of Biomedical Engineering, City University of Hong Kong, Tat Chee Avenue, Kowloon, Hong Kong, China*

(Received 18 December 2025; revised manuscript received 7 March 2026; accepted manuscript online 13 March 2026)

The combination of high-quality-factor (Q-factor) bound states in the continuum (BIC) and chiral metasurfaces has attracted much attention in the field of photonics. Here, we design and analyze a "sandwich" all-dielectric metasurface with two silicon cross-shaped cylinders distributed on the upper and lower surfaces of the silica. The transition from symmetry-protected BIC to chiral quasi-BIC (QBIC) is achieved by innovatively breaking both the mirror symmetry and the in-plane inversion symmetry of the structure, resulting in a transmittance-ratio circular dichroism (RCD) close to unity and a high Q-factor. In particular, three chiral QBICs (QBIC1, QBIC2, and QBIC3) are realized in the terahertz band without increasing the complexity of the structure at each layer. Multipole decomposition and near-field analysis demonstrate that QBIC1 and QBIC2 are dominated by the toroidal dipole and magnetic quadrupole, while QBIC3 is mainly affected by the electric quadrupole and magnetic quadrupole. In addition, the presence of positive and negative states due to the RCD values of the structure suggests a spin selectivity for different frequency bands. Theoretical assessment shows a maximum Q-factor of 3.94×10^4, a maximum sensitivity of 245 GHz per refractive index unit (RIU), and a figure of merit of 7927 RIU^{-1}. The results reveal a novel approach for selectively modulating circularly polarized light, demonstrating significant potential in biomolecular detection, high-spectral-resolution chiral biosensors, and chemical analysis.

Keywords: chiral quasi bound states in the continuum (QBIC), all-dielectric metasurfaces, circular dichroism, sandwich structure

PACS: 78.67.Pt, 42.25.Ja, 33.55.+b

DOI: 10.1088/1674-1056/ae516d **CSTR:** 32038.14.CPB.ae516d

1. Introduction

In the field of photonics, achieving a high quality factor (Q-factor) is important. Bound states in the continuum (BICs) are regarded as an effective method to obtain high Q-factors. These are localized non-radiative wave modes embedded in a continuous medium, characterized by zero linewidth and zero leakage,[1] and are widely used in diverse fields such as optical sensing and optoelectronic devices.[2] In metamaterials, there are two primary types of BICs: symmetry-protected BICs and Friedrich–Wintgen BICs.[3] BICs are essentially dark modes that do not couple with radiative waves.[4] To overcome the limitation of no coupling, BICs can be converted into quasi-BICs (QBICs) by breaking the symmetry, for example by modifying the structural geometry or changing the angle of the incident light. QBICs exhibit field-enhanced bright modes and sharp asymmetric Fano profiles in the spectrum, in addition to high Q-factors.[5,6] They also have a significant field enhancement effect, can reduce energy leakage and loss to improve the efficiency of optical processes, and offer a promising platform for advanced optical modulation.[7,8] The integration of chiral responses into optical metasurfaces has attracted increasing interest due to the interaction between circularly polarized light and chiral objects with different helicities.[9]

Chirality, a natural phenomenon in which an object differs from its mirror image, gives rise to unique optical responses on metasurfaces.[10] Introducing QBICs into chiral structures generates pronounced chiral optical responses and leads to distinct interactions with left- and right-circularly polarized (LCP/RCP) light, resulting in circular dichroism (CD) that can be characterized by measuring the differential light–structure interactions.[11–15] On chiral optical metasurfaces, chiral QBICs enable high-Q resonance and enhance light–matter interactions. This enhancement amplifies the differential response between LCP and RCP light, giving rise to a markedly pronounced CD with high potential for applications such as biosensing, optical detection, and quantum information processing.[16–18] By precisely designing and controlling BICs and chiral structures, selective control of LCP and RCP light can be achieved, consequently paving the way for the de-

[†]Corresponding author. E-mail: lvjingwei2009123@126.com

© 2026 Chinese Physical Society and IOP Publishing Ltd. All rights, including for text and data mining, AI training, and similar technologies, are reserved.

velopment of novel optical devices and technologies.[19,20]

Tailoring the structure and parameters of metasurfaces enables precise modulation of the polarization, phase, and amplitude of light to improve the chiral response.[21] For example, Cao *et al.* have designed metasurfaces made of asymmetrical silicon ellipse pairs. Two QBIC-driven chiral resonances are excited with a maximum CD of 0.91 and a Q-factor of 7196.[22] Sun *et al.* have considered a single cell composed of split-ring resonators by modifying the angle of incidence of the circularly polarized light, resulting in external chirality with a maximum CD of 0.17.[23] Shi *et al.* have proposed metasurfaces with α-Si columns by introducing in-plane structural asymmetry, showing a maximum CD of 0.99 and a Q-factor exceeding 390 at optical frequencies.[24] However, most studies on chiral metasurfaces have focused on achieving chiral QBICs by breaking the out-of-plane symmetry or perturbing the mirror symmetry. The design and realization of chiral metasurfaces capable of simultaneously attaining both a high Q-factor and a high CD remain challenging and require systematic investigation.

Herein, a two-layer chiral metasurface of cross-shaped silicon cylinders is designed. By simultaneously breaking the in-plane and mirror symmetry of the "sandwich" structure, high Q values as well as transmittance-ratio circular dichroism (RCD) are achieved. The numerical results show that the RCD of this sandwich structure exhibits both positive and negative forms, with a maximum RCD of 0.995 and a maximum Q-factor of 3.94×10^4. The maximum sensitivity (S) is 245 GHz per refractive index unit (RIU) and the figure of merit (FOM) is 7927 RIU^{-1}. Notably, we demonstrate higher sensitivity and FOM than in prior works. The contributions of magnetic quadrupole (MQ), toroidal dipole (TD), and electric quadrupole (EQ) modes to the three chiral QBICs are analyzed by multiple field analysis and decomposition. The effects of structural parameters on RCD are investigated by numerical simulation. The all-dielectric metasurface is shown to achieve near-unity RCD, high Q-factors of several orders of magnitude, and enhanced localized fields. The linewidth (i.e., spectrally selective) and chirality (i.e., spin-selective) of the metasurface can be flexibly tuned by varying the chiral asymmetry. The results establish a practical framework for terahertz radiation modulation of chiral all-dielectric metasurfaces, which have high potential in terahertz sensing systems.[25,26]

2. Theory and model

2.1. Structure and modeling

The two-layer cross-shaped cylinder structure is depicted in Fig. 1(a): two cross-shaped silicon cylinders are asymmetrically arranged on the top and bottom surfaces of the silica substrate. Compared with structures having rectangular cross sections, less mesh accuracy is required. The reduced precision needed for meshing results in lower losses, improved efficiency, and higher process robustness.[27] The substrate lattice is $P_x = P_y = P = 300$ μm, its thickness is $H = 130$ μm, and the refractive index is 1.46. The refractive index of the model structure is 3.7, and the symmetric metasurface is shown in Fig. 1(b). To obtain a chiral QBIC, both the in-plane symmetry and the mirror symmetry are broken so that the four arm lengths of the cross-shaped cylinder become $L_1 = L - 1.5\alpha$, $L_2 = L - 0.5\alpha$, $L_3 = L + 0.5\alpha$, and $L_4 = L + 1.5\alpha$, where $L = 54$ μm, and the width of the arms is $W = 36$ μm. In the symmetry-breaking process, the positions of L_1 and L_3 are interchanged, while the structural parameters of the cross-shaped cylinder remain unchanged. The top view of the symmetric and asymmetric structure of a single unit is presented in Fig. 1(c). We set periodic boundary conditions in the x and y directions and a perfectly matched layer in the z direction to absorb the reflected wave energy. The theoretical analysis is performed using the finite-element frequency-domain solver.

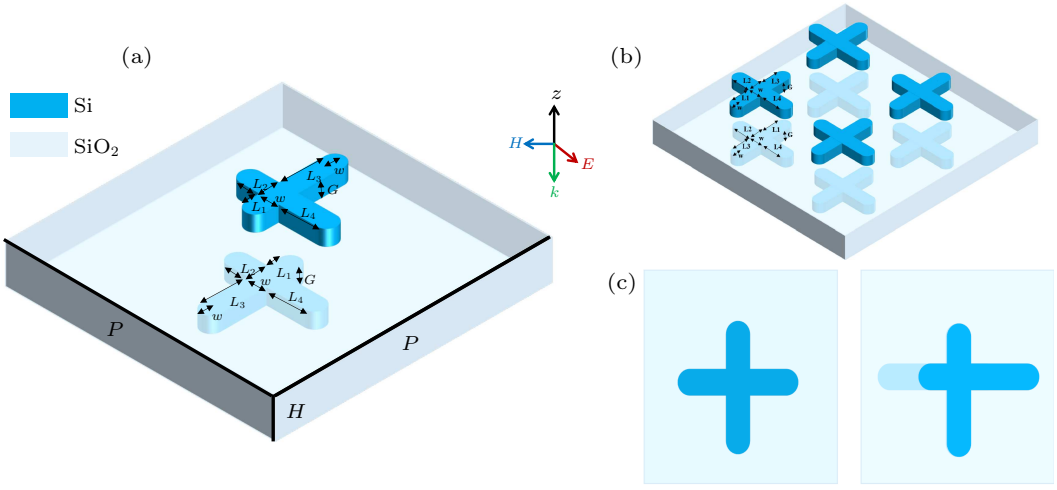


Fig. 1. (a) Single asymmetric metasurface, (b) symmetric metasurface, and (c) top view of symmetrical and asymmetrical structures.

2.2. Multipole decomposition

To elucidate the mechanisms of the three chiral QBIC modes, multipole decomposition is adopted. It can be categorized into the electric dipole (ED), magnetic dipole (MD), EQ, MQ, and TD modes,[28,29] which are represented by the following expressions:

$$P = \frac{1}{\mathrm{i}\omega}\int j\,\mathrm{d}^3 r, \tag{1}$$

$$M = \frac{1}{2c}\int (r\times j)\,\mathrm{d}^3 r, \tag{2}$$

$$T = \frac{1}{10c}\int \left[(r\times j)\,r - 2r^2 j\right]\mathrm{d}^3 r, \tag{3}$$

$$Q_{\alpha\beta} = \frac{1}{2\mathrm{i}\omega}\int \left[r_\alpha j_\beta + r_\beta j_\alpha - \frac{2}{3}(r\cdot j)\,\delta_{\alpha\beta}\right]\mathrm{d}^3 r, \tag{4}$$

$$M_{\alpha\beta} = \frac{1}{3c}\int \left[(r\times j)_\alpha\, r_\beta + (r\times j)_\beta\, r_\alpha\right]\mathrm{d}^3 r, \tag{5}$$

where j represents the current density, c is the speed of light, ω is the angular frequency, and P, M, $Q_{\alpha\beta}$, $M_{\alpha\beta}$, and T are the ED, MD, EQ, MQ, and TD moments, respectively.[30,31] Equations (1)–(5) show the different multipole contributions to far-field scattering.

2.3. Fano fitting

To demonstrate that the asymmetric parameter α and the Q-factor exhibit an inverse quadratic relationship with $Q = 1/\alpha^2$, the Fano model fit is applied to the transmittance curve T for calculation, as shown below:[32,33]

$$T = T_0 + G\frac{\left[q + 2(\omega-\omega_0)/\Gamma\right]^2}{1+\left[2(\omega-\omega_0)/\Gamma\right]^2}, \tag{6}$$

where T_0 is the background transmittance, G is the continuum-discrete coupling constant, q is the asymmetry factor, i.e., the Breit–Wigner–Fano parameter, $\omega = 2\pi c/\lambda$ is the resonant angular frequency, λ is the resonance wavelength, c is the speed of light in a vacuum, and Γ is the resonant linewidth.

3. Results and discussion

3.1. Analysis of the chiral QBIC model

When the cross-shaped cylinder possesses symmetry with a displacement parameter $\alpha = 0$ μm (arm length $L_1 = L_2 = L_3 = L_4 = L$), the transmission spectra of all Jones matrix elements are as shown in Fig. 2(a). Typically, the transmission of terahertz circularly polarized waves can be represented by a Jones matrix. This Jones matrix is represented as follows:[34,35]

$$J_{\mathrm{circ}} = \begin{pmatrix} t_{\mathrm{RR}} & t_{\mathrm{RL}} \\ t_{\mathrm{LR}} & t_{\mathrm{LL}} \end{pmatrix}, \tag{7}$$

where t_{ij} (i = R, L; j = R, L, where R denotes RCP and L denotes LCP) denotes the transmission coefficient from the input polarization j to the output polarization i, and the transmittance is given by $T_{ij} = |t_{ij}|^2$. T_{LL} and T_{RR} denote the polarizations under the incidence of LCP and RCP, respectively, and T_{LR} and T_{RL} denote the cross-polarizations. Since the symmetry of the structure is not broken, the configuration exhibits mirror symmetry but lacks chirality. Consequently, LCP and RCP light undergo the same physical interactions with the structure.[36] Since no distinct excitation modes or energy relations are generated, the transmission properties of LCP and RCP are identical, as manifested in the transmission spectra by coincident T_{LL} and T_{RR} curves.

In order to obtain a chiral QBIC, both the in-plane symmetry and mirror symmetry are broken. The transmission spectrum at a displacement parameter $\alpha = 10$ μm is shown in Fig. 2(b). For $\alpha = 0$ μm, the transmission spectrum remains nearly constant at 0.76–0.80 THz. Although this frequency range shows a BIC with infinite Q, it is not observed in the transmission spectrum due to its non-radiative nature. When the cross-shaped cylinder metasurface is shifted by $\alpha = 10$ μm, three resonance modes appear at frequencies of 0.7614 THz, 0.7768 THz, and 0.7928 THz (marked as QBIC1, QBIC2, and QBIC3). The orange and green lines indicate the transmission properties under RCP and LCP incidence and reflect the ability of the structure to modulate the transmission of light with different polarization states.[37,38] The purple solid line and the blue dashed line indicate cross-polarization of the incident light when $T_{\mathrm{LR}} = T_{\mathrm{RL}} \neq 0$, indicating the presence of cross-polarization. The CD response originates from the differential interaction of the chiral metasurface with LCP and RCP, resulting in distinct transmission peaks for the two polarizations. From the simulated energy band structure maps and Q-factor trends in Figs. 2(c) and 2(d), it is evident that the bands labeled red, green, and blue represent the symmetry-protected BICs at the Γ point, which supports three symmetry-protected BICs. Figures 2(e)–2(g) show the calculated Q-factors at different degrees of asymmetry for QBIC1, QBIC2, and QBIC3, all exhibiting the same inverse quadratic trend as described by the formula $Q = k\alpha^{-2}$, where k is a constant.

To determine the physical mechanism, the far-field scattering and near-field electromagnetic field distribution at $\alpha = 10$ μm were investigated. At $\alpha = 10$ μm, the contour plots of the electromagnetic field at different cross sections of QBIC1, the fitting plots of the Fano model, and the multipole decomposition are shown in Figs. 3(a)–3(d). As shown in Fig. 3(a), the total scattering rate of this mode is primarily attributed to TD, followed by MQ. To further elucidate the mechanism of the Fano resonance, Fig. 3(b) shows the Fano model fitting of QBIC1 at $\alpha = 10$ μm, indicating that the Fano model prediction (red curve) agrees well with the transmission rate (black line) around the resonance frequency. Figure 3(c) shows the electric field distribution in the x–y plane, and the two black arrows in Fig. 3(c) indicate displacement currents in two dif-

ferent directions. The white ring-shaped displacement current connects the two ring-shaped magnetic fields in different directions, as shown in Fig. 3(d), corroborating the existence of the MQ and TD modes. The near-field electromagnetic field distribution of QBIC1 is consistent with the multipole decomposition results in Fig. 3(a), further verifying that this mode stems from the combined contribution of the TD and MQ modes.

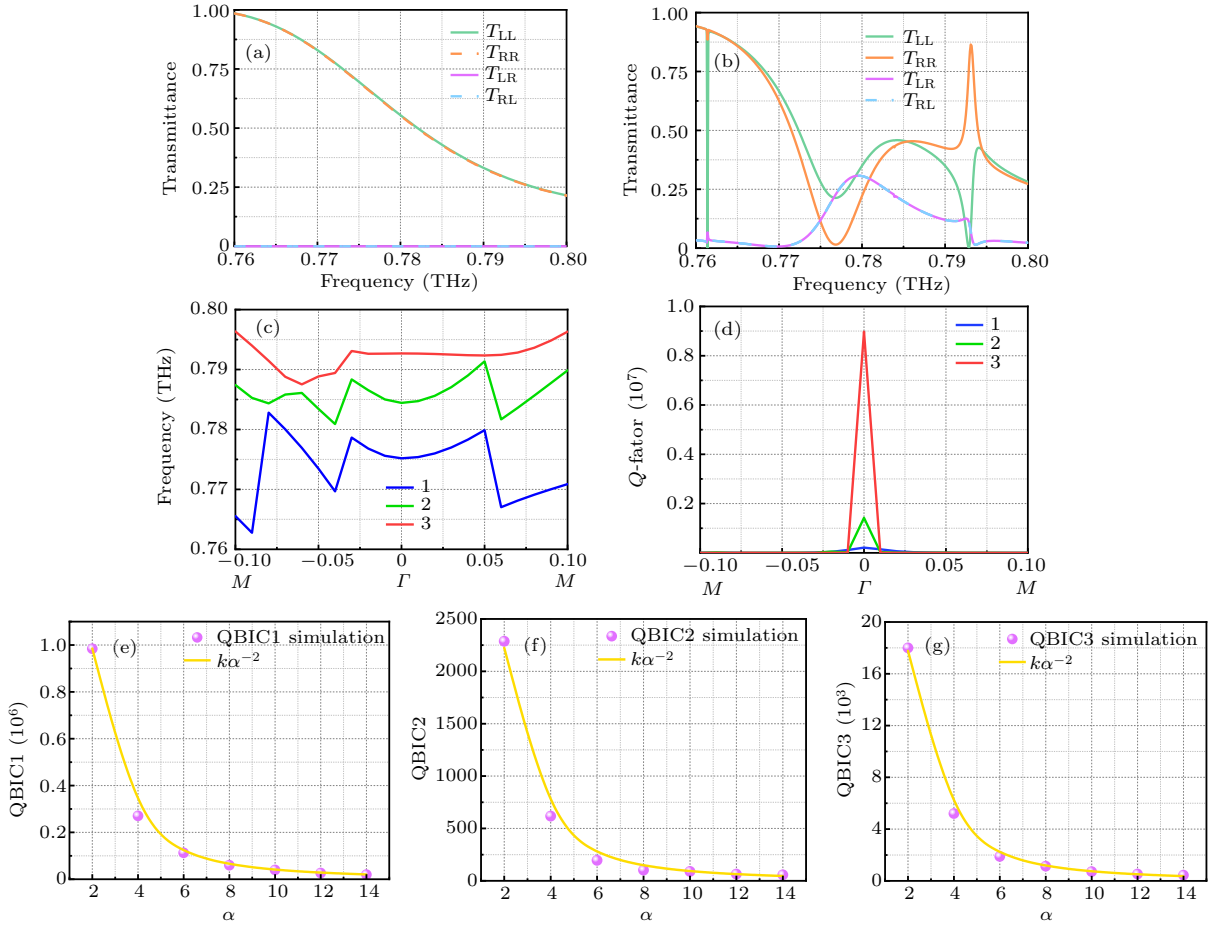


Fig. 2. (a) Transmission spectra in the symmetric case. (b) Transmission spectra with $\alpha = 10$ μm. (c) Simulated energy band structure with real parts of the eigenfrequency near the Γ-point. (d) Q-factor trend near the Γ-point. Q-factor as a function of degree of asymmetry α (e) for BIC1, (f) BIC2, and (g) BIC3.

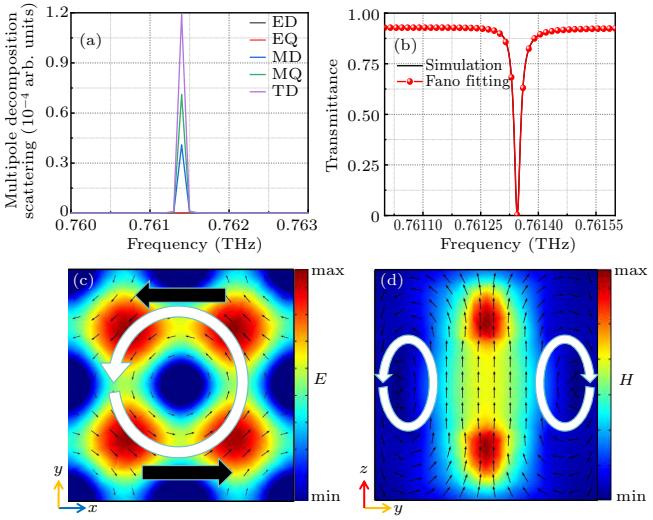


Fig. 3. (a) Multipole decomposition. (b) Fano fitting. (c) x–y, $z = 0$ μm cross-section, electric field distribution of QBIC1 at $\alpha = 10$ μm. (d) y–z, $z = 150$ μm cross-section, magnetic field distribution of QBIC1 at $\alpha = 10$ μm.

Figures 4(a)–4(d) show the multipole decomposition, Fano fitting, and electromagnetic field maps at $\alpha = 10$ μm. Figure 4(a) shows that the QBIC2 mode is primarily influenced by the TD and MQ modes. Figure 4(b) presents the Fano fitting curve to provide information about the interactions and coupling mechanisms between different modes on the optical metasurface. It shows the Fano model fitting of QBIC2 at $\alpha = 10$ μm, indicating that the Fano model prediction agrees well with the transmission rate around the resonance frequency. Figure 4(c) shows the electric field distribution at the y–z cross-section at $x = 150$ μm, and Fig. 4(d) shows the magnetic field distribution at the x–z cross-section at $y = 150$ μm. The electric field intensity of the QBIC2 mode is primarily distributed at the interface between the structure and the substrate. At this location, two counter-directed ring-shaped displacement currents are formed (white ring-shaped arrows in Fig. 4(c)). Combined with the ring-shaped magnetic vectors at the central position in Fig. 4(d), this demonstrates that the mode is influenced by the TD mode. Figure 4(d) shows two magnetic vectors with completely different directions on both sides (two black arrows), proving the existence of the MQ

mode. Based on the above analysis, the electromagnetic fields of the multipole modes in Figs. 4(c) and 4(d) are consistent with the equipotential line diagram of the multipole contributions in Fig. 4(a), indicating that the scattering efficiency of the QBIC2 mode is jointly influenced by the TD and MQ modes.

Figures 5(a)–5(e) show the multipole decomposition, Fano fitting, surface charge distribution, and electromagnetic field distribution of QBIC3 at $\alpha = 10$ μm. Figure 5(a) is the multipole decomposition diagram, showing that the QBIC3 mode is primarily dominated by the EQ mode, followed by the MQ mode, while other modes have negligible effects. Figure 5(b) is the Fano fitting diagram, where the fitted curve closely matches the simulated curve. Figure 5(c) is the x–y surface charge distribution diagram, with four pairs of positive and negative charges symmetrically coupled, indicating the presence of the EQ mode. Figure 5(d) is the y–z cross-section electric field diagram at $x = 150$ μm, showing four displacement currents with opposite directions distributed at the contact surfaces between the upper and lower structures and the substrate. Combined with Fig. 5(e), the x–z cross-section magnetic field distribution diagram at $y = 81$ μm and $y = 199$ μm, the four magnetic vectors of different directions confirm the presence of the MQ mode. By comprehensively analyzing the multipole decomposition and the electromagnetic field distribution diagrams, QBIC3 is jointly dominated by the EQ and MQ modes.

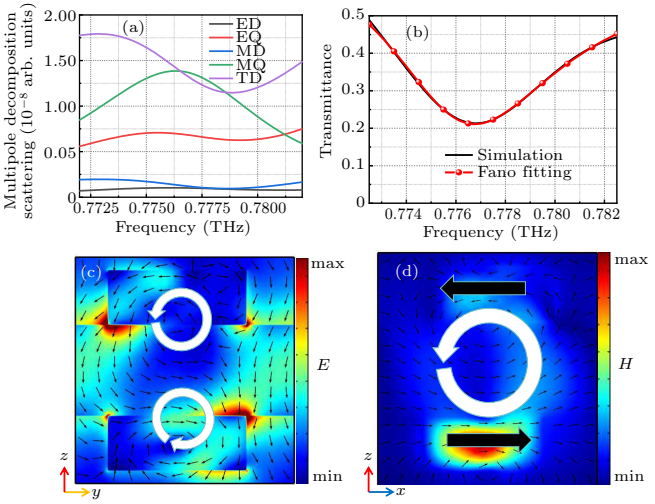


Fig. 4. (a) Multipole decomposition. (b) Fano fitting. (c) y–z, $x = 150$ μm cross-section, electric field distribution of QBIC2 at $\alpha = 10$ μm. (d) x–z, $y = 150$ μm cross-section, magnetic field distribution of QBIC2 at $\alpha = 10$ μm.

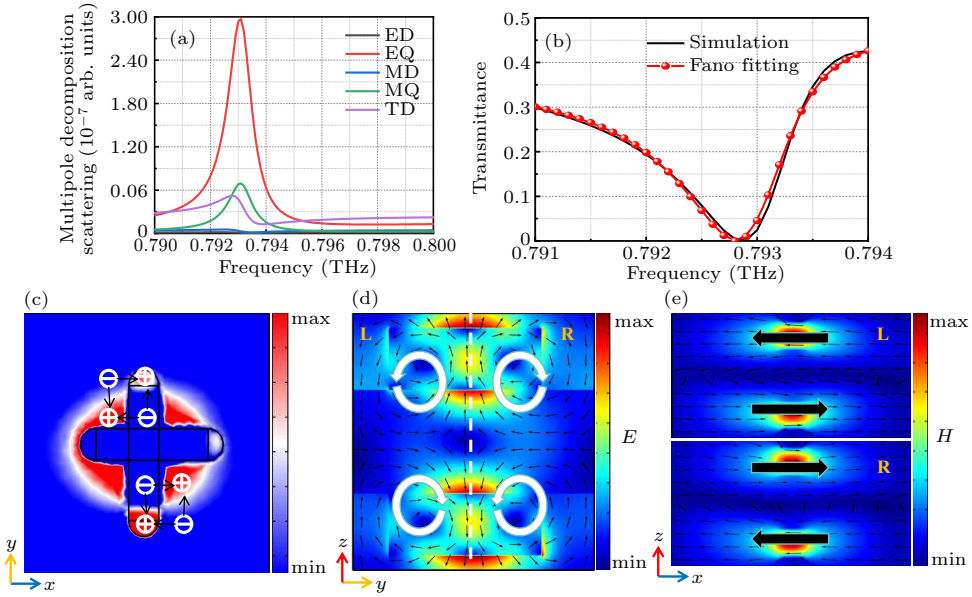


Fig. 5. (a) Multipole decomposition. (b) Fano fitting. (c) Surface charge distributions. (d) y–z, $x = 150$ μm cross-section, electric field distribution of QBIC3 at $\alpha = 10$ μm. (e) x–z, $y = 81$ μm (L) and $y = 199$ μm (R) cross-section, magnetic field distribution of QBIC3 at $\alpha = 10$ μm.

3.2. Analysis of structural parameters of chiral QBIC models

To illustrate the influence of structural parameters on chiral QBIC-induced CD, the following parameters were chosen: $P = 300$ μm, $W = 36$ μm, $G = 76$ μm, $L = 54$ μm, and $H = 130$ μm. The offset $\alpha = 10$ μm remains constant. The chiral response is obtained by varying each parameter individually. The CD is calculated using a normalized transmittance-based formula, which more clearly reflects the selectivity between LCP and RCP light. All CDs reported in the text are defined using transmittance ratios, referred to as transmittance-ratio CDs (RCDs). In order to prevent the situation where transmittance is low for both LCP and RCP light, we have also evaluated the average transmittance (T_{avg}) as follows:[9,39–41]

$$\mathrm{RCD} = \frac{\mathrm{LCP_T} - \mathrm{RCP_T}}{\mathrm{LCP_T} + \mathrm{RCP_T}}, \tag{8}$$

$$T_{avg} = \frac{\mathrm{LCP_T} + \mathrm{RCP_T}}{2}, \tag{9}$$

where $\mathrm{LCP_T}$ ($\mathrm{RCP_T}$) is the transmittance under LCP (RCP) incidence.

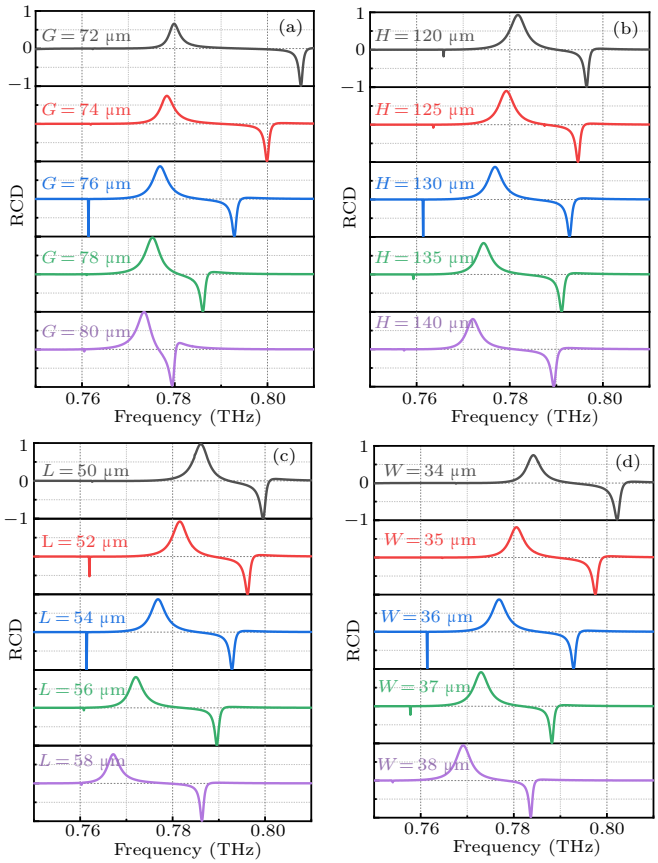


Fig. 6. Circular dichroism of metamaterial transmission: (a) effects of cross-shaped cylindrical thickness G on RCD spectra; (b) effects of substrate thickness H on RCD spectra; (d) effects of cross-shaped cylindrical arm length L on RCD spectra; (d) effects of cross-shaped cylindrical arm width W on RCD spectra.

As shown in Fig. 6, the regularity of the transmitted wave depends on changes in the structural or material parameters. Figure 6(a) shows the effects of different thicknesses G of the cross-shaped cylinder on the RCD. As G increases, the RCD of the QBIC1 mode gradually becomes evident, reaching a minimum value at $G = 76$ μm. Since the transmittance of linear LCP is lower than that of RCP, this indicates spin-selective transmission at different frequency bands, resulting in a negative RCD value. At this point, $\mathrm{RCD_{min}} = -0.996$. The center frequency of the RCD for the QBIC2 mode blueshifts slightly, and the RCD shows a gradually increasing trend, reaching a maximum at $G = 80$ μm with $\mathrm{RCD_{max}} = 0.995$. The large blueshift of QBIC3 causes the center frequencies of QBIC2 and QBIC3 to shift from mode 3 to mode 2. The RCD value of the QBIC3 mode first decreases and then increases, reaching a minimum value at $G = 74$ μm with $\mathrm{RCD_{min}} = -0.9997$. The RCD spectrum exhibits three inverse resonances, clearly indicating that the cross-shaped cylindrical metasurface has different chiral responses across multiple frequency bands. As the height of the structure G increases, the effective refractive index and equivalent optical range decrease, while due to the sandwich structure studied, it will modulate the relative phase of the coupling strength and the radiation channel, resulting in an elevated resonance frequency manifested as a blueshift. Figure 6(b) shows the effects of different thicknesses of the SiO_2 substrate H on the superstructure RCD. As H increases from 120 μm to 140 μm in 5 μm intervals, the effective optical cavity length between the upper and lower structures increases and the equivalent refractive index decreases, resulting in a higher resonance frequency and an overall blueshift. The RCD of the QBIC1 mode reaches a minimum at $H = 130$ μm, with $\mathrm{RCD_{min}} = -0.996$. The RCD spectrum of the QBIC2 mode gradually decreases, reaching a maximum at $H = 120$ μm, with $\mathrm{RCD_{max}} = 0.928$. The RCD value of the QBIC3 mode continuously increases, with $\mathrm{RCD_{min}} = -0.998$ at $H = 120$ μm. To investigate the effects of arm length on the chiral response of the cross-shaped cylindrical structure, the changes in the RCD spectrum are analyzed as the arm length L increases from 50 μm to 58 μm. When the structural arm length L is increased, the electromagnetic energy distribution of the unit and the equivalent boundary conditions are reconstructed, which reduces the effective refractive index and shortens the equivalent optical range; at the same time, the increase in L will change the near-field coupling strength and the phase matching relationship between the upper and lower layers, which leads to elevation of the resonance frequency and the occurrence of a blueshift. The RCD value of QBIC1 reaches its minimum at $L = 54$ μm with $\mathrm{RCD_{min}} = -0.996$. The RCD values of QBIC2 and QBIC3 both reach their maximum and minimum at $L = 50$ μm, with $\mathrm{RCD_{max}} = 0.973$ and $\mathrm{RCD_{min}} = -0.9996$, respectively. Figure 6(d) shows the effects of the arm width W on the structural RCD, with the arm width gradually increasing from 34 μm to 38 μm (increasing by 1 μm each time). In this process, the confinement of the electric and magnetic fields in the transverse direction is increased, causing all resonant modes to exhibit significant blueshifting. The QBIC1 mode shows the minimum RCD value at $W = 36$ μm, with $\mathrm{RCD_{min}} = -0.996$. At $W = 38$ μm, the QBIC2 mode exhibits the maximum RCD value, $\mathrm{RCD_{max}} = 0.945$. When $W = 37$ μm, the QBIC3 mode reaches its minimum RCD value, with $\mathrm{RCD_{min}} = -0.998$. Therefore, the different couplings between the cross-shaped cylindrical metasurface structures and LCP and RCP waves produce different chiral responses at different frequencies. QBIC1 is a TD-dominated QBIC, and geometric perturbations continuously tune the coupling and leakage, while QBIC2 and QBIC3 are EQ-dominated or multichannel hybrid QBICs, and geometric perturbations asymmetrically change the multipole interference and LCP/RCP coupling difference, resulting in stronger and more complex changes in RCD. Compared with QBIC1, QBIC2 and QBIC3 have larger radiative losses leading to Q limitation, while QBIC3 is dominated by EQ, and its mode coupling to free-space radiation is more likely to be turned on

in the presence of structural asymmetry. Therefore, we need to enhance the radiative cancellation to suppress the residual low-order radiative components and reduce the additional leakage due to substrate asymmetry and processed scattering.

To investigate the strong chiral response of the cross-shaped cylindrical structure, the transmission spectra for LCP and RCP incidence under three chiral QBIC modes with the maximum absolute value of RCD are shown in Figs. 7(a)–7(f). When $\alpha = 10$ μm, Figs. 7(a) and 7(b) show the transmission spectra and RCD spectra of QBIC1 for $G = 76$ μm, $H = 130$ μm, $L = 54$ μm, and $W = 34$ μm. Owing to the significant difference in transmission rates between LCP and RCP, the RCD of QBIC1 reaches its minimum value at this point, with $\mathrm{RCD_{min}} = -0.996$. Figures 7(c) and 7(d) show the transmission spectrum and RCD spectrum at $G = 80$ μm, $H = 130$ μm, $L = 54$ μm, and $W = 34$ μm. The transmission rate for LCP is higher than that for RCP. At this point, the RCD of QBIC2 exhibits a positive value, with a maximum $\mathrm{RCD_{max}} = 0.995$. Figures 7(e) and 7(f) show the transmission diagram and RCD spectrum for $G = 74$ μm, $H = 130$ μm, $L = 54$ μm, and $W = 34$ μm. The RCD of QBIC3 exhibits a negative value, with $\mathrm{RCD_{min}} = -0.9997$. To avoid practical issues that may arise when the transmittance under either LCP or RCP incidence approaches zero, we further analyzed the average transmittance for LCP and RCP, as shown in Fig. 7(g). In addition, Fig. 7(h) illustrates the dependence of the structure's RCD on α for different values of the asymmetry parameter. As α increases, the center frequencies of the RCD in the three chiral QBIC modes do not shift significantly. However, the linewidths of the QBIC2 and QBIC3 modes gradually increase, exhibiting a trend of shifting toward the QBIC3 mode. Accordingly, the significant difference in transmittance between the two different spin states indicates a strong intrinsic chiral response on the chiral metasurfaces.[42–44]

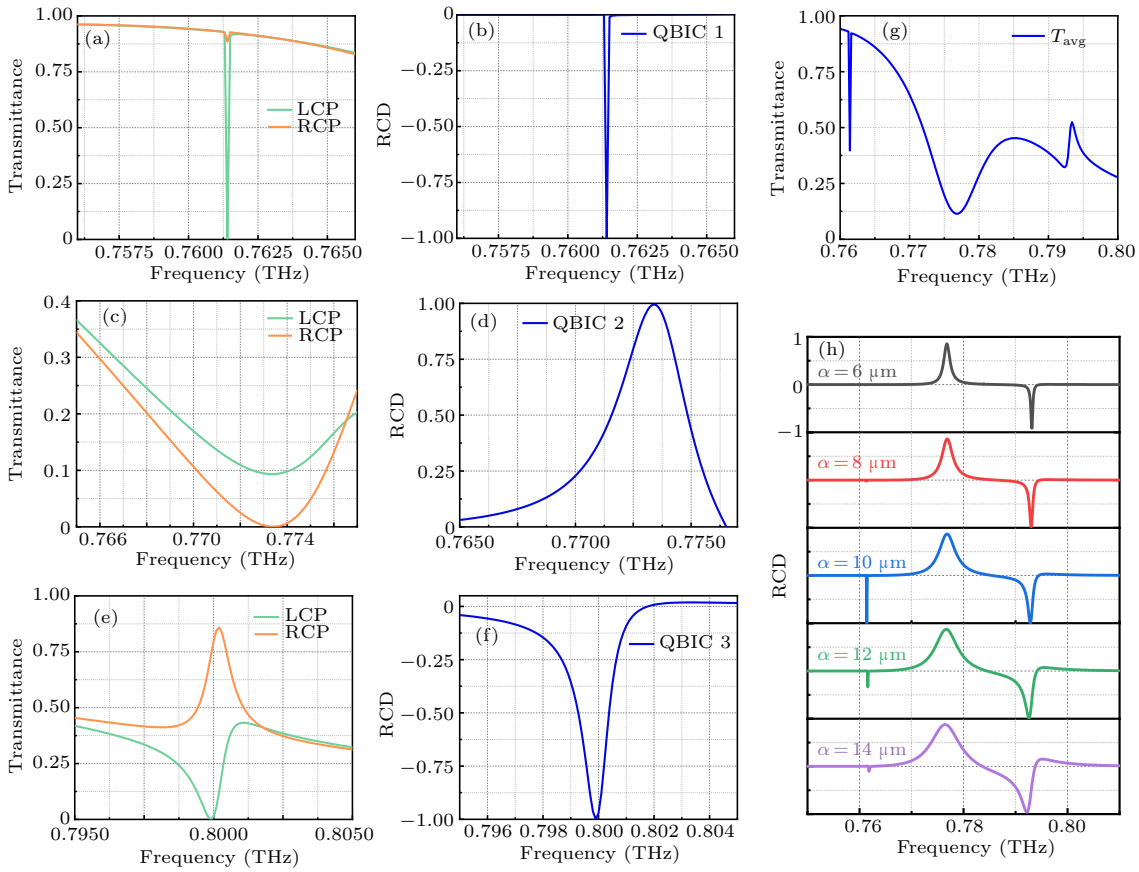


Fig. 7. Transmittance and RCD spectra under LCP and RCP incidence for different chiral QBIC modes: (a), (b) transmittance and RCD spectra of QBIC1; (c), (d) transmittance and RCD spectra of QBIC2; (e), (f) transmittance and RCD spectra of QBIC3;(g) average transmittance under LCP and RCP; (f) effects of different asymmetry parameters α on the RCD of the structures.

3.3. Analysis of sensing characteristics of chiral QBIC models

For ultra-high sensitivity, significant progress has been achieved with extensive applications in fields such as biosensors and environmental monitoring. Consequently, we investigated the sensing performance of the proposed metasurface. Due to its narrow full width at half maximum (FWHM) and RCD approaching unity, it can detect minute variations in the refractive index of the surrounding environment. Its sensitivity S and FOM are expressed by the following formulae:[45]

$$S = \frac{\Delta f}{\Delta n}, \tag{10}$$

$$\mathrm{FOM} = \frac{S}{\mathrm{FWHM}}, \tag{11}$$

whereΔn is the change in refractive index and Δf is the shift of the center frequency with Δn.

We investigated the RCD as a function of the environmental refractive index n ranging from 1.00 to 1.04. As shown in Fig. 8(a), all three chiral QBICs exhibit a blue shift with increasing refractive index n. To quantify the sensitivity of the proposed structures, the refractive indices corresponding to the band positions of the three QBICs were fitted linearly, as depicted in Fig. 8(b). The maximum coefficient of determination R^2 in the figure can reach 100%. The fitting results indicate that the maximum S is 245 GHz/RIU from QBIC3. The sensitivity advantage of QBIC3 comes from its stronger interfacial electric field with a larger ambient field energy share, and the sensing sensitivity is dominated by the ambient coupling weights rather than by the Q value alone. The maximum FOM is 7927 RIU^{-1}.

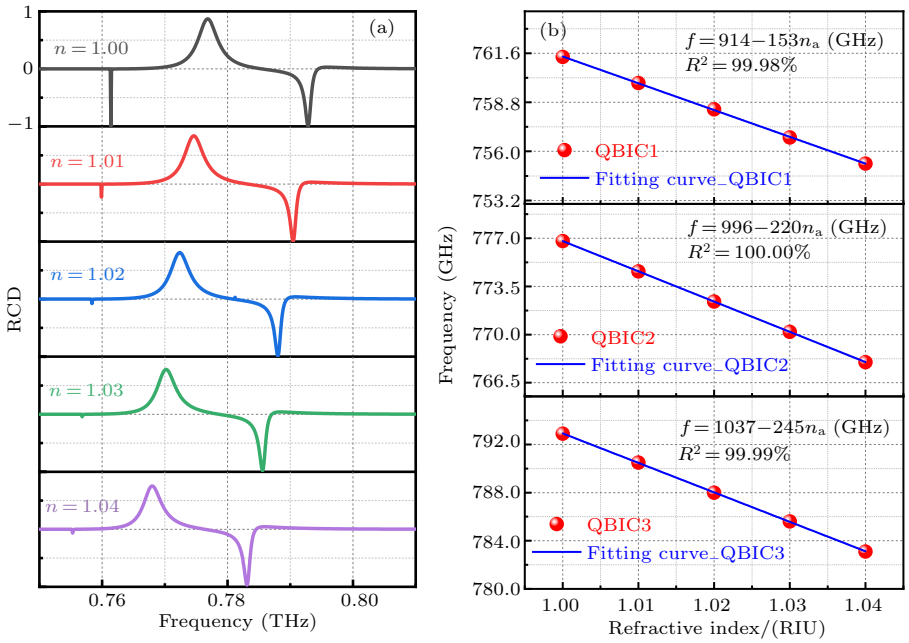


Fig. 8. (a) RCD spectra for refractive indexes going up from 1.00 to 1.04. (b) Linear fitting of QBICs and refractive index.

In summary, our cross-shaped cylindrical metasurfaces achieve a high Q and a chiral response, RCD, in the terahertz band, showing three chiral QBICs without introducing complex interlayer structures. The field-enhanced nature of the high-Q resonance makes the device more sensitive to ambient refractive index and weak chiral perturbations, which significantly improves the sensing frequency modulation efficiency and reduces the detection limit. By optimizing the structural parameters, we have also achieved dynamic tuning of the device performance, including sensitivity and circular dichroism. A comparison of our results with previous ones reveals that this structure has a superior high Q and a giant chiral response, as shown in Table 1.

Table 1. Comparison of chiral responses between our design and those reported recently.

Reference	Material	Waveband	CD	Q-factor	S	FOM
[46]	Si	938–940 nm	0.98	3216	47.9 nm/RIU	163 RIU^{-1}
[47]	Si	8.4–9.9 GHz	∼	2303	67 GHz/RIU	7023 RIU^{-1}
[22]	Si	49–54 THz	0.91	7196	12.87 THz/RIU	1371 RIU^{-1}
[48]	Au	0.1–0.7THz	0.52	4.45	39.4 GHz/RIU	–
[49]	Si	1470–1500 nm	0.94	2×10^4	136.2 nm/RIU	1135 RIU^{-1}
This work	**Si**	**0.75–0.81 THz**	>0.99	3.94×10^4	**245 GHz/RIU**	**7927 RIU^{-1}**

4. Conclusion

In this work we designed and analyzed a double-layer all-dielectric cross-shaped cylindrical structure metasurface. By simultaneously breaking the planar symmetry and mirror symmetry of this structure, three chiral QBICs were generated in the terahertz frequency band. Numerical simulation disclosed a pronounced chiral response and high Q-factors, showing a maximum Q-factor of 3.94×10^4, S of 245 GHz/RIU and FOM

of 7927 RIU^{-1}. By analyzing the effects of different structural parameters on the RCD spectra, the irradiance, linewidth and operating frequency of the chiral response can be tuned flexibly. The thickness of the cross-shaped cylindrical structure affects the coupling between the upper and lower structures. The electromagnetic field distribution of each mode was analyzed in detail, and the dominant role of TD, MQ and EQ modes in chiral QBICs analyzed by multilevel decomposition as well as near-field distribution. The variability of the transmission spectra under LCP and RCP incidence leads to spin-selective transmission of RCD in different frequency bands, while $RCD_{max} = 0.995$ and $RCD_{min} = -0.999$ were obtained. The cross-shaped cylindrical double-layer metasurface structure presents a new design and solution for spin-selective transmission in multiple terahertz bands with high potential in chiral optics and chiral biosensors with high Q values.

Appendix A: Processing steps

Figure A1 illustrates the fabrication procedure for the metasurface. Prior to fabrication, the fused silica substrates were cleaned with acetone to remove organic contaminants, followed by rinsing with isopropyl alcohol and deionized water to eliminate residual oil, dust, and other surface impurities. After the cleaning process, silicon films were deposited onto the SiO_2 substrates using low-pressure chemical vapor deposition (LPCVD). To address the low electrical conductivity of the SiO_2 substrate, the Si film was subsequently coated with ZEP520 photoresist and AR-PC conductive adhesive. Electron beam lithography (EBL) was then employed to define the metasurface pattern in the photoresist layer. After resist development, pattern fixation, and etching, the samples were immersed in acetone to remove the conductive adhesive. Finally, the samples were rinsed with deionized water and dried under a nitrogen flow to prevent the formation of watermarks.[50,51]

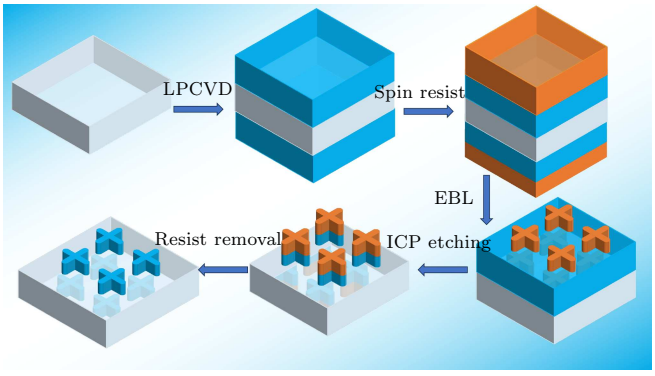


Fig. A1. Processing steps for metasurface fabrication.

Acknowledgements

The work was jointly supported by the National Natural Science Foundation of China (Grant No. 12304480), Heilongjiang Provincial Natural Science Foundation of China (Grant No. JQ2023F001), and City University of Hong Kong Donation Research Grants, China (DON-RMG 9229021 and 9220061).

References

[1] Chern R L, Kao S W and Lin P Y 2025 *Opt. Express* **33** 16863
[2] Tian H, Li J, Wu Y and Wang X 2025 *Opt. Commun.* **574** 131181
[3] Lv J, Ren Y, Wang D, Wang J, Lu X, Yu Y, Li W, Liu Q, Xu X, Liu W, Chu P K and Liu C 2024 *Opt. Express* **32** 28334
[4] Lamayny K, Harroui F Z, El Abouti O, Mrabti T, Amrani M, Khattou S, Labdouti Z, Mouadili A and El Boudouti E H 2024 *Phys. Lett. A* **519** 129722
[5] Koshelev K, Lepeshov S, Liu M, Bogdanov A and Kivshar Y 2018 *Phys. Rev. Lett.* **121** 193903
[6] Liu J Q, Zheng Y, Li X, Li J W, Zhang G H, Dong D X, Liu D M, Jia Y W, Fu Y Y and Liu Y W 2025 *Chin. Phys. B* **34** 074208
[7] Zhou M, You S, Xu L, Fan M, Huang J, Ma W, Hu M, Luo S, Rahmani M, Cheng Y, Li L, Zhou C, Huang L and Miroshnichenko A E 2023 *Sci. China Phys., Mech. Astron.* **66** 124212
[8] Ma W and Zhou C 2023 *Opt. Lett.* **48** 2158
[9] Xie S, Sun S, Shen W, Yang J, Guan X, Chen J, Zeng Z and Sun M 2024 *J. Lightwave Technol.* **42** 7765
[10] Wu J, Jiang H, Guo Z, Sun Y, Li Y and Chen H 2023 *Opt. Lett.* **48** 916
[11] Qi X, Wu J, Wu F, Zhao S, Wu C, Min Y, Ren M, Wang Y, Jiang H, Li Y, Guo Z, Yang Y, Zheng W, Chen H and Sun Y 2024 *Photonics Res.* **12** 244
[12] Tang H, Stan L, Czaplewski D A, Yang X and Gao J 2024 *Opt. Express* **32** 20136
[13] Chen B, Zhu W, Jiang H, Wang L, Zhou C and Zhang H 2025 *Opt. Lett.* **50** 3321
[14] Ji Y T, Chen S S, Gu C X and Li S G 2025 *Chin. Phys. Lett.* **42** 034202
[15] Wang B, Yan F, Liu X, Sun W and Li L 2024 *Opt. Express* **32** 8974
[16] Kim K H and Kim J R 2021 *Adv. Opt. Mater.* **9** 2101162
[17] Zhao W K, Wang S Y, Jing Y H, Ge H, Wang Q, Zeng Y Q, Jia B W and Xu N 2025 *Opt. Lett.* **50** 1649
[18] Zong S, Zeng D, Liu G, Wang Y, Liu Z and Chen J 2022 *Opt. Express* **30** 40470
[19] Luo C and Sang T 2025 *Opt. Laser Technol.* **184** 112500
[20] Ma T, Zou Y, Sang W, Ma L, Wang D and Li J 2025 *Opt. Laser Technol.* **184** 112423
[21] Yang H L, Ni B, Guo J H, Zhou H and Chang J H 2025 *Chin. Phys. B* **34** 050702
[22] Cao S, Sun P, Yu J, Wulan Q, Xing L, Liu Y and Liu Z 2025 *Appl. Opt.* **64** 1660
[23] Sun Y, He C, Deng Z, Li X, Li X, Zhang Z, Sui X, Li N, He W and Chen F 2025 *Nanophotonics* **14** 559
[24] Shi T, Deng Z L, Geng G, Zeng Y, Hu G, Overvig A, Li J, Qiu C W, Alu A, Kivshar Y S and Li X 2022 *Nat. Commun.* **13** 4111
[25] Aupiais I, Grasset R, Daineka D, Briatico J, Perfetti L, Hugonin J P, Greffet J J and Laplace Y 2024 *ACS Photonics* **11** 4184
[26] Zhang N, Zhang M, Ouyang Q and Chen L 2025 *TrAC, Trends Anal. Chem.* **191** 118360
[27] Rulff P, Buntin L M and Kalscheuer T 2021 *Geophysical Journal International* **227** 1624
[28] Zhou C, Li S, Wang Y and Zhan M 2019 *Phys. Rev. B* **100** 195306
[29] Liu Z, Wang B, Wang S, Du J, Chi Z and Li N 2024 *Opt. Laser Technol.* **177** 111140
[30] Lv J, Shi J, Ren Y, Wang D, Kong W, Liu Q, Li W, Yu Y, Wang J, Liu W, Chu P K and Liu C 2025 *Opt. Commun.* **574** 131162
[31] Hao Y and Yang R 2024 *Opt. Lett.* **49** 5819
[32] Wang P, He F, Liu J, Shu F, Fang B, Lang T, Jing X and Hong Z 2022 *Photonics Res.* **10** 2743

[33] Wang T, Liu S, Zhang J, Xu L, Yang M, Ma D, Jiang S, Jiao Q and Tan X 2024 *Nanophotonics* **13** 463
[34] Cao T, Wei C, Mao L and Li Y 2014 *Sci. Rep.* **4** 7442
[35] Ye W, Yuan X, Guo C, Zhang J, Yang B and Zhang S 2017 *Phys. Rev. Appl.* **7** 54003
[36] Du X, Xie S, Nan H, Sun S, Shen W, Yang J and Guan X 2023 *Photonics* **10** 980
[37] Gao Z, Wang P, Xu Z and Zhao T 2024 *Opt. Laser Technol.* **175** 110826
[38] Zhang Y, Hu T, Guo P and Li J 2025 *Phys. Rev. A* **112** 13513
[39] Liu Q S, Chao M H, Zhang W J and Song G F 2022 *Ann. Phys.* **534** 2200263
[40] Suchitta A, Suri P, Xie Z, Xu X and Ghosh A 2021 *Nanotechnology* **32** 315705
[41] Sha X, Du K, Zeng Y, Lai F, Yin J, Zhang H, Song B, Han J, Xiao S, Kivshar Y and Song Q 2024 *Sci. Adv.* **10** eadn9017
[42] Kong Y B, Sun X Y, Chen W W, Xu S T, Liu G Q and Wang Y H 2023 *Results Phys.* **54** 107075
[43] Zeng J, Zhou Y, Fu X, Yang J, Chen Y and Hong W 2025 *Opt. Express* **33** 27014
[44] Shi Y, Duan Y, Huang L, Chen W, Liu J and Wang M 2024 *Composites, Part B* **283** 111614
[45] Gorkunov M V, Antonov A A, Tuz V R, Kupriianov A S and Kivshar Y S 2021 *Adv. Opt. Mater.* **9** 2100797
[46] Li J, Duan Q, Dong X, Yang Z, Xie Z, Zhu S and Chen H 2024 *Phys. Rev. Appl.* **22** 44035
[47] Wang M, Zhao X, Zhao R and Lu G 2023 *Results Phys.* **49** 106518
[48] Chen X, Ye L and Yu D 2025 *IEEE Sensors J.* **25** 6301
[49] Cheng Y, Li J, Zeng D, Liu W, Liu Z and Liu G 2024 *Opt. Lett.* **49** 165
[50] Komarov F, Vlasukova L, Parkhomenko I, Milchanin O, Mudryi A, Togambaeva A and Korolik O 2015 *Thin Solid Films* **579** 110
[51] Chen Y F 2015 *Microelectronic Engineering* **135** 57